ACS OMEGA

http://pubs.acs.org/journal/acsodf

Article

Stabilization of the Nano-Sized 1T Phase through Rhenium Doping in the Metal–Organic CVD MoS_2 Films

Roman I. Romanov, Ivan V. Zabrosaev, Maxim G. Kozodaev, Dmitry I. Yakubovsky, Mikhail K. Tatmyshevskiy, Aleksey A. Timofeev, Natalia V. Doroshina, Sergey M. Novikov, Valentyn S. Volkov, and Andrey M. Markeev*

Cite This: *ACS Omega* 2023, 8, 16579–16586

Read Online

ACCESS | Metrics & More | Article Recommendations | Supporting Information

ABSTRACT: Heterogeneous nanostructures composed of metastable tetragonal 1T-MoS_2 and stable hexagonal 2H-MoS_2 phases are highly promising for a wide range of applications, including catalysis and ion batteries, due to the high electrical conductivity and catalytic activity of the 1T phase. However, a controllable synthesis of stabilized 1T-MoS_2 films over the wafer-scale area is challenging. In this work, a metal–organic chemical vapor deposition process allowing us to obtain ultrathin MoS_2 films containing both 1T and 2H phases and control their ratio through rhenium doping was suggested. As a result, $Mo_{1-x}Re_xS_2$ films with a 1T-MoS_2 fraction up to ≈30% were obtained, which were relatively stable under normal conditions for a long time. X-ray photoelectron spectroscopy and Raman spectroscopy also indicated that the 1T-MoS_2 phase fraction increased with rhenium concentration increase saturating at Re concentrations above 5 at. %. Also, its concentration was found to significantly affect the film resistivity. Thus, the resistivity of the film containing approximately 30% of the 1T phase was about 130 times lower than that of the film without the 1T phase.

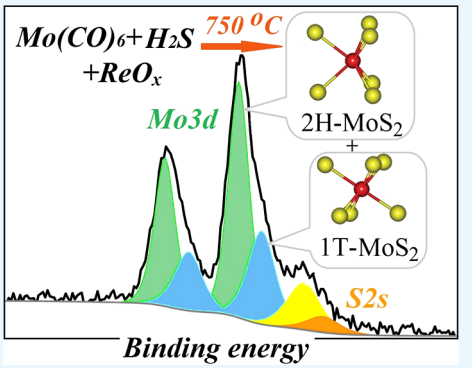

INTRODUCTION

Two-dimensional (2D) transition metals dichalcogenides (TMDCs), in particular MoS_2, represent a specific class of layered materials where neighboring layers are bonded by the weak van der Waals forces. In most cases, TMDCs exist in the form of films containing multiple stable molecular layers with atomically smooth chemically inert surfaces, which naturally results in a number of their outstanding properties.[1−3] Such films are of interest for nanoelectronic and optoelectronic applications,[4,5] photovoltaics,[6,7] photodetectors,[8,9] and gas sensors.[10,11] On the other hand, TMDCs may also be prepared in a significantly different form with a high specific surface area and high density of chemically active surface states, which makes them promising for catalysis,[12−16] ion batteries,[17] and supercapacitors.[18] Three MoS_2 crystalline phases are known, hexagonal (2H), rhombohedral (3R), and tetragonal (1T) with a different coordination of sulfur atoms to molybdenum, which determine the chemical and electronic properties of the material. The 3R-MoS_2 and 1T-MoS_2 phases are metastable and may transform into 2H-MoS_2 under certain conditions.[19] One of the specific features of the 1T-MoS_2 phase is metallic conductivity, attributed to the fact that there are only two electrons at the triply degenerate t_{2g} orbital of the Mo4d level.[19] Another 1T-MoS_2 distinctive feature is improved catalytic activity owing to the active basal states compared to only edge atoms being active in the 2H phase,[20] which is attractive for catalysis applications, in particular the hydrogen evolution reaction.[21] However, obtaining the 1T phase in MoS_2 films was found to be challenging. One of the possible mechanisms of its synthesis is chemical or electrochemical exfoliation by alkali metal intercalation, accompanied by the electron transfer from the alkali ion to the d-orbital of molybdenum. As a result, the 1T phase becomes more stable compared to the 2H one, but the phase transition is incomplete. Also, the resulting 1T phase is very fragile due to weak interaction between neighboring sulfur layers.[22] To improve its stability, doping or intercalation by the electron-donating metal atoms was suggested,[19,23,24] but the intermediate Li_xMoS_2 and the intercalator of *n*-butyllithium are hazardous and pyrophoric materials.[19] Besides the aforementioned intercalation approach, the 2H-1T phase transition may also be induced by electron beam irradiation,[25] plasmonic hot injection,[26] or direct hydrothermal synthesis.[27] The obtained 1T/2H-MoS_2 heterogeneous structures are significantly more stable than the pure 1T-MoS_2 phase, while the phase coexistence grants their unique properties. In addition to enhanced electrical conductivity and catalytic state density,

Received: October 21, 2022
Accepted: April 19, 2023
Published: May 3, 2023

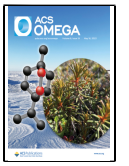

https://doi.org/10.1021/acsomega.2c06794
ACS Omega 2023, 8, 16579–16586

high photoresponse and external quantum efficiency were demonstrated for a photodetector, consisting of the top 2H-MoS_2 and bottom 1T/2H-MoS_2 layers.[28] However, the aforementioned synthesis techniques are either quite complex or time-consuming. In this regard, the development of a technological approach that makes it possible to obtain ultrathin films consisting of a combination of 1T/2H-MoS_2 phases, which are stable over a wide temperature range, is still of great practical interest. Up to date, most of the reported results correspond to the 2H-MoS_2 synthesis by chemical vapor deposition (CVD),[29−31] physical deposition,[32] or two-step sulfurization.[33−35] Among them, metal−organic CVD (MOCVD) recently attracted a great deal of attention because it allows for electronic grade films' uniform deposition over wafer-scale areas and demonstrates the highest controllability.[36]

Direct 1T-MoS_2 CVD fabrication is extremely challenging due to its thermodynamic instability. However, 1T phase formation was reported in monolayer CVD $Mo_{1-x}W_xS_2$ deposited onto substrates with a thermal expansion coefficient higher than that of MoS_2 and WS_2 films.[37] In this case, transition to the 1T phase is induced by compressive thermal strains. A number of studies mention Re doping utilization for 1T-MoS_2 phase stabilization.[19,38,39] Such treatment provides excess electrons that fill the Mo higher energy levels (d_{xy}, $d_{x^2-y^2}$), which leads to the transformation of the 2H structure into 1T.

In this work, we report an original MOCVD MoS_2 film doping method through use of ReO_x particles as the rhenium precursor. Moreover, specific MOCVD growth regimes were employed with a low molybdenum precursor concentration and high S/Mo concentration ratio in the gas phase, which allowed for ultrathin $Mo_{1-x}Re_xS_2$ film synthesis containing the metastable 1T phase. As a result, the influence of the deposition process parameters on the 1T-MoS_2 fraction in the stabilized heterogeneous 1T/2H-MoS_2 structure was investigated.

EXPERIMENTAL SECTION

At the first stage, rhenium oxide was deposited in a three-zone tube furnace HZS-1200 (Carbolite Gero) equipped with a 32 mm outer diameter quartz tube in the air. A crucible containing metallic rhenium (10 g, 99.9% purity) was placed in the center of the heated zone of the tube. Sapphire substrates were placed at the edge of the heated area, where the temperature varied from 240 to 130 °C as shown in Figure S1a. The furnace was heated up to 310 °C and maintained at this temperature for 10 min. Then, the heaters were turned off, allowing the furnace to cool down. At the second stage, the MOCVD processes were carried out in a homemade reactor based on a three-zone tube furnace HZS-1200. Molybdenum hexacarbonyl $Mo(CO)_6$ (99.98% purity, Sigma-Aldrich) and hydrogen sulfide (H_2S) were used as precursors, while the Ar + 5% H_2 mixture was used as the carrier gas. $Mo(CO)_6$ was kept in a stainless-steel bubbler held at a temperature of 21.5 °C. The calculated outlet gas flow rates of $Mo(CO)_6$ were 1.5×10^{-3} sccm, 2.5×10^{-3} sccm, and 4.1×10^{-3} sccm, while the flow rate of H_2S (99.9%) was 15 sccm for all samples. The Ar + 5% H_2 carrier gas flow rate was 600 sccm, which resulted in a working pressure of 25 mBar. The process temperature was fixed at 750 °C. The growth time varied from 2 to 6 h in order to obtain continuous films at various flow rates of $Mo(CO)_6$. In particular, at the $Mo(CO)_6$ flow of 1.5×10^{-3} sccm, the continuous monolayer MoS_2 film is formed after about 3 h. Cleaned (piranha solution, deionized water) 20 × 10 mm-size sapphire pieces were used as substrates. Immediately prior to the MOCVD process, the sapphire substrates were annealed for an hour in the air at 1000 °C. The annealing process was carried out at the same three-zone tube furnace which was used for the CVD process. It should be noted that every stage, including ReO_x deposition, substrate annealing, and MOCVD MoS_2 deposition, was carried out in a separate quartz tube.

The deposition process was carried out as follows: Annealed sapphire substrates were placed in the central zone of the tube furnace. Substrates with pre-deposited rhenium oxide obtained at the first stage were placed upstream in the tube, toward the gas inlet (Figure S1b). The system was pumped down to a pressure below 0.1 hPa prior to the start of the process. The heating step was carried out in a continuous carrier gas flow with a temperature ramp rate of 30 °C/min. When the temperature set point was reached, H_2S was supplied to the reactor, and after 10 min of stabilization time, $Mo(CO)_6$ flow was supplied as well. After the growth process, the heating system was switched off, allowing the furnace to cool down. During the cooling process, down to 450 °C, the H_2S flow was maintained. Below this point, only carrier gas was supplied. In general, a series consisting of 7 samples further named by a combination of $Mo(CO)_6$ flow, process time, and rhenium treatment was fabricated (see Table S1 for the description). After the growth, samples were annealed under high-vacuum (2×10^{-6} mBar) conditions (T = 200 °C) for 2 h to remove the sulfur excess.

The films' chemical state and composition were analyzed by X-ray photoelectron spectroscopy (XPS) in a Theta Probe spectrometer (Thermo Scientific) with a monochromatic Al-Kα X-ray source (1486.6 eV). For such analysis, the grown films were immediately transferred from the furnace to the XPS load lock and pumped down to a pressure of 1.5×10^{-7} mBar for about 20 min and then transferred to the analysis chamber kept at a pressure of 2.0×10^{-9} mBar. Photoelectron spectra were acquired using the fixed analyzer transmission mode with 50 eV pass energy under the charge compensation mode.

The films' morphology was examined by atomic force microscopy (AFM) on an NT-MDT NTEGRA tool in a semi-contact mode using a silicon tip with a radius <10 nm (HA-NC, SCANSENS). To measure film thickness, it was successively immersed in KOH solution and water and then transferred onto a pristine substrate, where the step profile was measured by AFM (Figure S2 represents the data measured for the Mo1.5−3 film). The film structural analysis was performed on a Tecnai G2transmission electron microscope operated at an accelerating voltage of 200 kV. Raman spectroscopy was used to get insights into the detailed film structure. A LabRAM Evolution (Horiba Scientific) instrument with a 532 nm laser source with 1 cm^{-1} spectral resolution was used to perform the spectral measurements. A diffraction grating of 1800 lines/mm and a 100× objective lens (numerical aperture = 0.90) were utilized in these experiments. The laser spot diameter was 0.45 μm. The laser intensity was kept below 0.5 mW to ensure that laser-induced heating does not introduce artifacts. The film sheet resistance was estimated by a four-probe method using a Keysight B1500A measurement unit connected to a Cascade Microtech Summit probe station with DCP-HTR tungsten probes. The resistance was measured at five different points for each sample.

https://doi.org/10.1021/acsomega.2c06794
ACS Omega 2023, 8, 16579−16586

RESULTS AND DISCUSSION

Figure S3 presents the AFM image of a sapphire substrate covered with rhenium oxide particles, which was used in the consequent MOCVD process. These particles ranged in size from about 10 to 300 nm. In Figure S4, the XPS spectrum of Re4f core levels of this sample is provided. The spectrum was decomposed into two doublets. The major one with a binding energy (BE) of line $Re4f_{7/2}$ of 46.2 eV corresponds to the Re_2O_7 compound. An additional doublet with a BE of line $Re4f_{7/2}$ of 43.6 eV corresponds to ReO_2. In order to control the result reproducibility, each sample with rhenium oxide was investigated using AFM and XPS techniques prior its use in the MoS_2 MOCVD process. Figure 1 presents the AFM image of

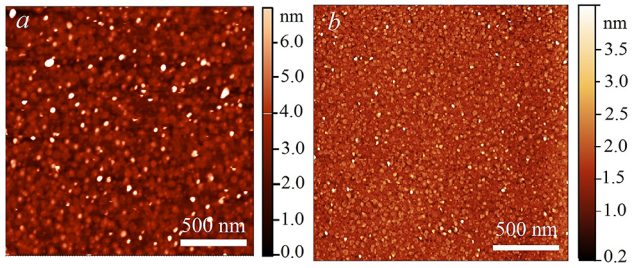

Figure 1. AFM image of Mo2.5-4 (a) and Mo2.5-4-Re (b) films.

Mo2.5-4 and Mo2.5-4-Re samples, which demonstrates a fine-grained continuous film, with a grain size of several tens of nanometers. For the rhenium-doped sample, slight grain size decrease is observed. The estimated root-mean-square value for these samples was calculated to be 0.38 and 0.23 nm, respectively.

Transmission electron microscopy (TEM) analysis (Figure S5) revealed that the investigated film is polycrystalline with an average grain size of 30−50 nm. The analysis of the corresponding high-resolution TEM image (Figure 2) shows

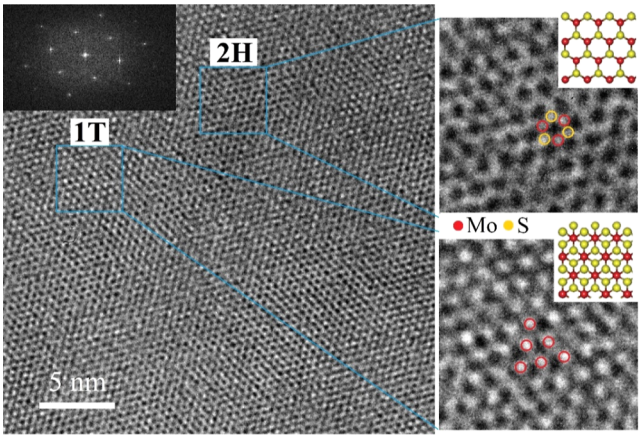

Figure 2. Plan-view high-resolution TEM images of the Mo2.1-4 film.

that the crystalline structure is locally distorted due to the presence of point defects. Moreover, as the close investigation of the areas in blue frames suggests, several regions are characterized by a trigonal lattice (octahedral coordination), which is a clear fingerprint of the 1T phase, while other regions have a honeycomb lattice (trigonal prismatic coordination) of the 2H phase.

In Figures 3−5, XPS spectra of Mo3d, S2p, and Re4f core levels for Mo1.5-6, Mo1.5-6-Re, Mo2.5-4-Re, and Mo4.1-2-Re films are presented. All spectra were decomposed into two doublets. For Mo3d spectral decomposition, the first doublet with a BE of the $Mo3d_{5/2}$ line of 229.6−229.7 (eV) and a spin−orbit splitting of 3.15 eV is typical of the 2H structure. The second one with a BE for the $Mo3d_{5/2}$ line of 228.7−228.8 (eV) and similar spin−orbit splitting is associated with the 1T structure, which confirms the TEM analysis result (Figure 3).[20] For the corresponding S2p decompositions, the first doublet with a BE for the $S2p_{3/2}$ line of 162.5−162.6 eV and a spin−orbit splitting of 1.1 eV corresponds to the 2H structure,[39] while the second one with a BE of 161.6−161.7 eV is associated with the 1T phase (Figure 4). The Re4f spectrum was decomposed into the doublets with a BE of line $Re4f_{7/2}$ of 41.4 eV (corresponding to the 2H structure) and 40.5 eV (corresponding to the 1T structure) (Figure 5).[39] In addition, a weak $Re4f_{7/2}$ doublet is observed in the spectra, with a BE of approximately 45.4−45.7 eV, corresponding to ReO_3 or Re_2O_7 oxides. The fraction of oxidized rhenium is estimated to be 7−8%. The phase composition estimation based on these spectra resulted in a 0, 31, 28, and 17% relative 1T phase fraction for Mo1.5-6, Mo1.5-6-Re, Mo2.5-4-Re, and Mo4.1-2-Re films, respectively. The Re concentration for the respective samples was found to be 0, 8, 5, and 3 (at. %). Moreover, the estimated [S]/([Mo] + [Re]) ratio was found to be 2.1−2.2 for the films under investigation, which exceeds the stoichiometric ratio. The additional annealing under high-vacuum conditions (2×10^{-6} mBar) at 200 °C for 2 h resulted in its decrease to the nominal value (2), which was accompanied by a slight Mo3d and S2p line constriction. Therefore, we believe that such a procedure allowed us to remove the excess sulfur.

Raman spectroscopy was employed for additional structural analysis and to further confirm 1T-MoS_2 phase presence (Figure 6). In the 120 to 500 cm^{-1} range, Raman spectra have a series of peaks corresponding to different MoS_2 phases. Since the exciting radiation wavelength of 532 nm is not resonant, only first-order peaks $E_{2g}{}^1$ (383 cm^{-1}) and A_{1g} (405 cm^{-1}) should be observed in a perfect 2H-MoS_2 lattice spectrum. However, at higher $Mo(CO)_6$ flow and for films with the rhenium component, weak peaks appear in the low-frequency region corresponding to the crystal lattice defects. The most intense of them [LA(M)] is observed at 227 cm^{-1}. These peculiarities arise from a small crystalline domain size because they are known to be sensitive to lattice defects[40] and nanoparticle size.[41] For the films containing Re, besides the 2H phase peaks, the discussed spectra also contain a series of peaks at 150 cm^{-1} (J1), 220 cm^{-1} (J2), and 325 cm^{-1} (J3) and the peak at 285 cm^{-1} (E_{1g}), which confirm the 1T phase presence.[16,20,39] As Figure 6 demonstrates, as $Mo(CO)_6$ flow decreases, the intensity of the peaks corresponding to the 1T-MoS_2 phase increases, whereas $E_{2g}{}^1$ and A_{1g} peak intensity, corresponding to the 2H-MoS_2 phase, decreases. In addition, these peaks broaden and shift toward lower-wavenumber values by 1 cm^{-1}. In the Mo1.5-6-Re sample spectrum, weak peaks are observed at 160 and 305 cm^{-1}, which likely correspond to E_g-like vibrational modes in the ReS_2 structure.[42]

Thus, when samples with ReO_x particles are placed in the reactor during the MOCVD process, the deposited MoS_2 film is doped by rhenium. With increased $Mo(CO)_6$ flow, the MoS_2 film deposition rate increased, whereas the rhenium concentration was maintained at the same level in each process. As a

https://doi.org/10.1021/acsomega.2c06794
ACS Omega 2023, 8, 16579−16586

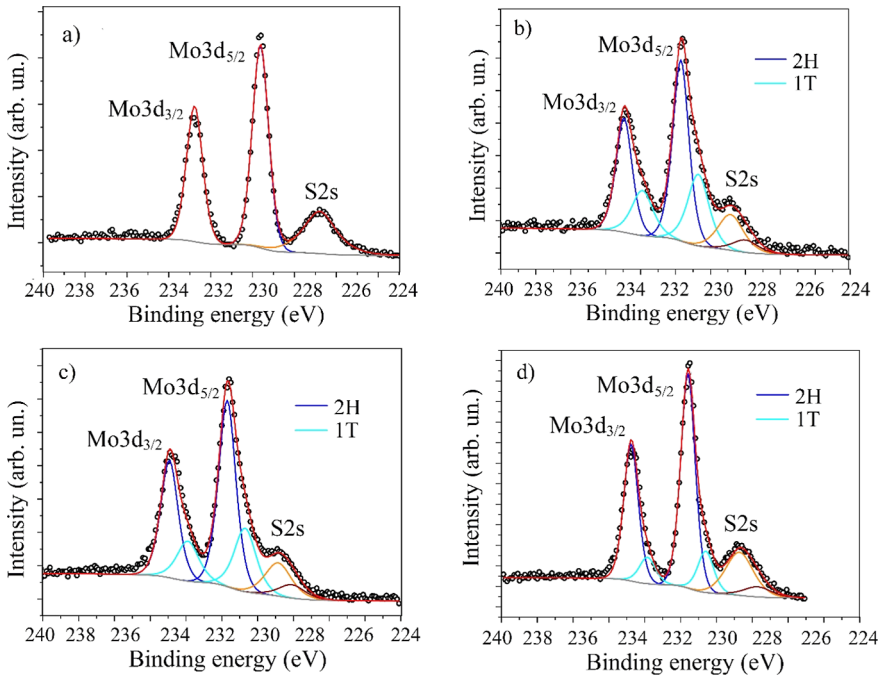

Figure 3. XPS core-level Mo3d spectra of grown Mo $_{1-x}Re_xS_2$ films: Mo1.5-6 (a), Mo1.5-6-Re (b), Mo2.5-4-Re (c), and Mo4.1-2-Re (d).

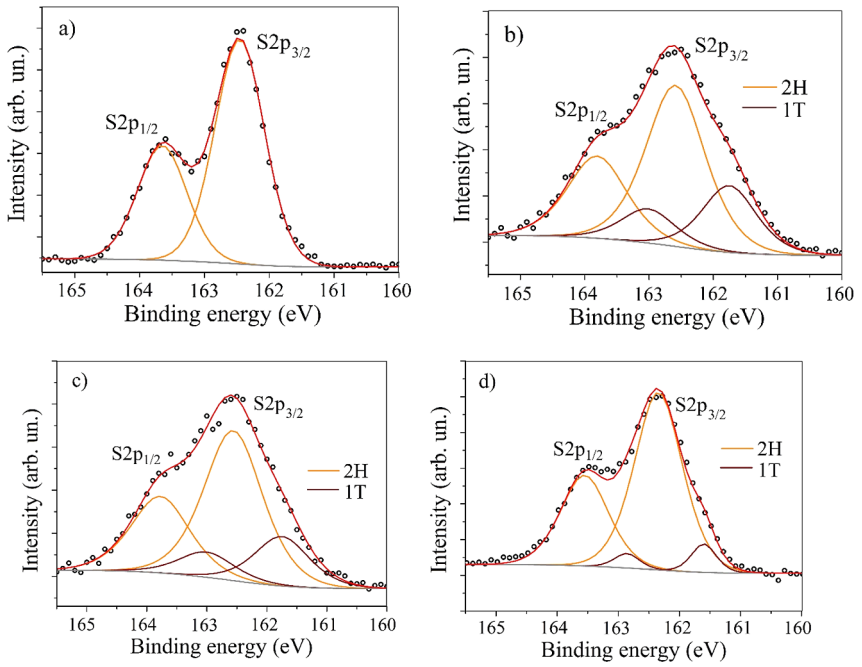

Figure 4. XPS core-level S2p spectra of grown Mo $_{1-x}Re_xS_2$ films: Mo1.5-6 (a), Mo1.5-6-Re (b), Mo2.5-4-Re (c), and Mo4.1-2-Re (d).

result, the rhenium concentration in films is lower at higher $Mo(CO)_6$ flow. XPS investigation results suggest that for rhenium-doped films, Re and Mo atoms are found in chemical states characteristic of both 2H and 1T phases. With the increased rhenium concentration in films, the 1T-MoS_2 phase fraction also increases. The maximal 1T-MoS_2 phase fraction (31%) corresponds to the maximal Re concentration. However, with the rhenium concentration increasing from 5 to 8 (at. %), 1T fraction increase is significantly weaker, indicating saturation. On the contrary, the rhenium 1T-ReS_2 fraction decreases with the increased Re concentration. The maximal fraction was found to be 65%.

The structural difference of the samples also manifested itself in photoluminescence spectra (Figure 7). Mo1.5-5 and Mo2.5-4 spectra demonstrate the main peak at 1.88−1.86 eV corresponding to A-excitons and a weakly expressed shoulder peak at 1.95 eV, corresponding to B-excitons.[43,44] In the sample Mo1.5-6-Re spectrum, the intensity of the peak corresponding to A-excitons is considerably lower than that in other samples, its position is shifted toward higher energies (1.92 eV), and the shoulder peak at 2.1 eV corresponding to B-excitons is more distinct.

The synthesized heterogeneous structures containing 1T and 2H phases are stable under ambient conditions without

https://doi.org/10.1021/acsomega.2c06794
ACS Omega 2023, 8, 16579−16586

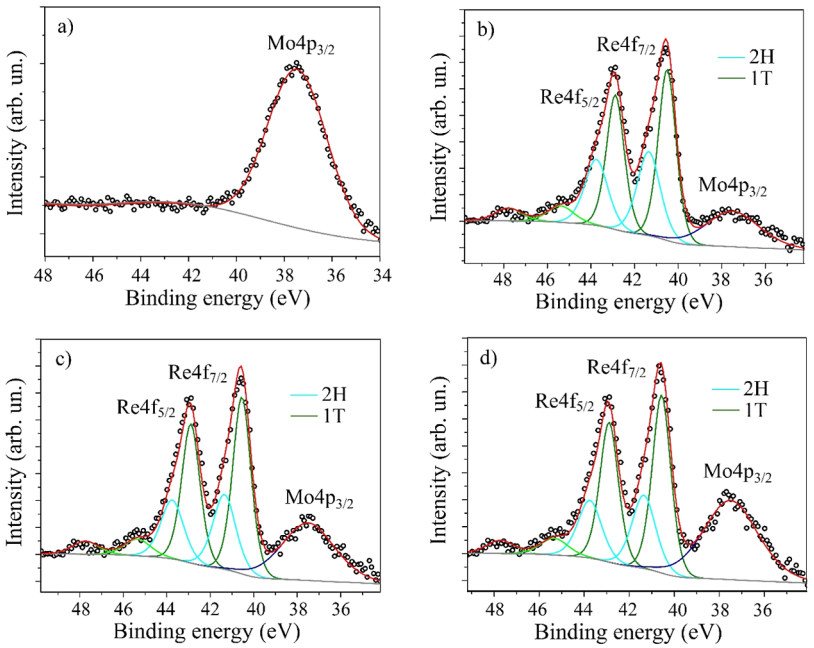

Figure 5. XPS core-level Re4f spectra of grown Mo $_{1-x}$Re$_x$S$_2$ films: Mo1.5-6 (a), Mo1.5-6-Re (b), Mo2.5-4-Re (c), and Mo4.1-2-Re (d).

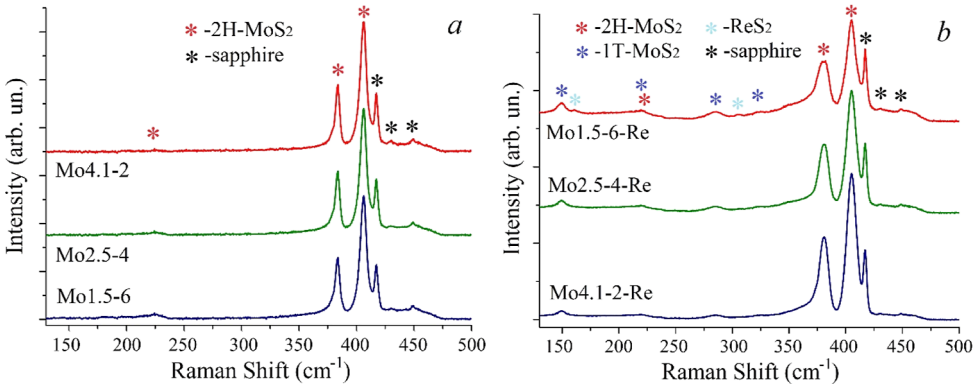

Figure 6. Raman spectra of MoS_2 (a) and Mo $_{1-x}$Re$_x$S$_2$ (b).

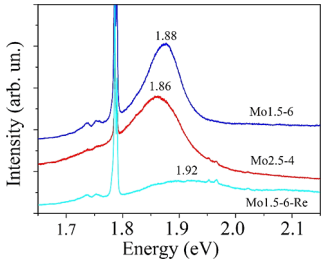

Figure 7. Photoluminescence spectra of Mo1.5-6, Mo2.5-4, and Mo1.5-6-Re films.

performance degradation in not less than 4 months and withstand annealing in high vacuum at a temperature of up to 300 °C. We also confirmed the film uniformity over the substrate by Raman spectroscopy (Figure S6). Since the measured $I(E_{1g})/I(A_{1g})$ intensity ratio exhibited only small fluctuations across the investigated sample, the phase composition seems to be quite uniform. Because in this experiment we were limited only by the inner diameter of the laboratory-scale furnace, we believe that the developed MOCVD process is scalable on larger substrates if the conditions are optimized for a given equipment setup.

With respect to the literature data, the main applications of the obtained 1T/2H heterogeneous structures are related to catalysis and electronics but with several limitations on the substrate material. However, we do not see any fundamental limitation for employing the described method in the other substrates, which makes the results of potential interest for electronics. Often, a shortcoming of the synthesized 2H-MoS_2 films is a rather high resistance at MoS_2-metal contact, which limits the achievable I_{on} current in field-effect transistors (FETs). Since the 1T phase conductivity is ~10^7 times higher compared to that of the 2H one,[20] the film resistance may be tuned by changing the 1T phase concentration.

Therefore, the 1T phase influence on the films' electrical properties of four films with a different phase composition was also investigated: Mo1.5-6, Mo1.5-6-Re, Mo2.5-4-Re, and Mo4.1-2-Re. Specifically, the resistivity of these films was measured, and it was found that the measured values are quite uniformly distributed across the films' surface. In Figure 8, the averaged resistance for each investigated sample is provided depending on the E_{1g} to A_{1g} Raman peak intensity ratio which

https://doi.org/10.1021/acsomega.2c06794
ACS Omega 2023, 8, 16579−16586

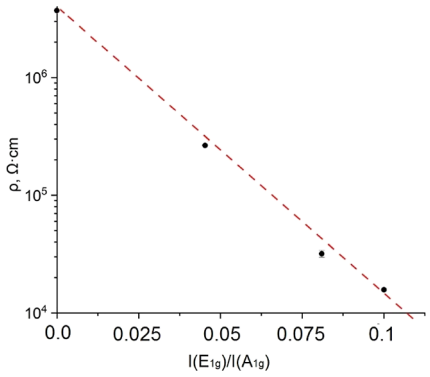

Figure 8. Resistivity dependence on the $I(E_{1g})/I(A_{1g})$ Raman peak ratio, corresponding to the 1T phase fraction.

is proportional to the 1T-MoS_2 fraction. As the figure suggests, the film resistivity anticorrelates with the fraction of the 1T-phase. Moreover, this dependence is exponential. One of the possible explanations for this fact is that the film's conductivity is determined by the density of highly-conducting 1T-MoS_2 grains, due to the changing average distance between them, as it is described in ref 45. However, for polycrystalline films studied in this work, the resistivity value should be governed by the film's structure with its high resistivity owing to the combination of relatively small crystalline size and high intergrain boundary resistance. We believe that this is the origin of high resistivity found in the studied films, which is 15 kΩ·cm for films with the highest 1T fraction and as high as 2 MΩ·cm for the film with the lowest 1T fraction. On one hand, the crucial role of the intergrain boundaries for polycrystalline TMDC films' conductivity is already well known.[46−48] On the other hand, sheet resistances reported for single nanosheets and flakes with induced 1T phase transition are significantly lower reaching hundreds of Ω/□ for the few-layered material.[49,50] The data directly relevant for the investigated films on synthesized large-area thin 1T-MoS_2 films' resistivity is lacking, as 1T-MoS_2 is unstable and challenging to fabricate.[20] In the work,[51] a resistivity of up to 1 kΩ·cm is reported for 1T MoS_2 nanosheets, consisting of coalesced overlapping grains. Another work[52] reports the significant resistance increase in a magnetron-deposited MoS_2 film, annealed at high temperatures, up to 8 MΩ/□ for a 50 nm film annealed at 900 °C. Authors suggest that this increase is caused by grain boundaries' formation, accompanying grain crystallization. Overall, we believe that substantially different film resistance in our structures is due to the polycrystalline structure of the material, which consists of poorly coalesced separate grains with a high intergrain resistance value.

CONCLUSIONS

In this work, the process of metastable 1T phase formation in MOCVD of rhenium-doped MoS_2 films was studied. The rhenium concentration was controlled by varying the Mo precursor flow rate. The concentration of the rhenium precursor in the form of samples with pre-deposited ReO_x particles was maintained constant. This method allows for film synthesis over the large scale. Deposition regimes were determined, allowing us to fabricate the films with nanoscale 1T-MoS_2 and 2H-MoS_2 domains. XPS and Raman spectroscopy investigation suggests that the 1T-MoS_2 fraction increases with the increasing Re concentration, attributed to $Mo_{1-x}Re_xS_2$ film growth rate decrease. At a Re concentration above 5 at. %, saturation is observed. The maximal 1T-MoS_2 fraction obtained is 30% at a Re concentration of 8 at. %. At this concentration, ReS_2 phase formation indications are observed. Octahedral coordination in MoS_2 is assumed to be formed due to higher electron density, induced by excess electrons at the Re outer d-shell. Fabricated heterogeneous 1T/2H-MoS_2 films remain stable under ambient conditions without performance degradation for at least 4 months and withstand high-vacuum annealing at 300 °C. These films might also be of interest for electronic applications as increase of the 1T phase fraction is shown to decrease films' resistivity; it was found to be 130 times less for the film without 1T-MoS_2 than that for the film with the 30% 1T fraction.

ASSOCIATED CONTENT

Supporting Information

The Supporting Information is available free of charge at https://pubs.acs.org/doi/10.1021/acsomega.2c06794.

ReO_x deposition scheme and MOCVD MoS_2 deposition scheme; growth conditions and resulting MoS_2 film thicknesses; AFM image of the Mo1.5−3 film edge (measured thickness profile); AFM image of a sapphire substrate covered with rhenium oxide particles used in the consequent MOCVD process; XPS spectrum of Re4f core levels of the sapphire substrate, covered with ReO_x particles; bright-field (SAED pattern) and dark-field TEM images of the Mo2.5-4-Re film; and Raman spectra of the Mo2.5-4-Re film at different points across the sample and E_{1g}/A_{1g} intensity ratio as a function of the measurement point coordinate (PDF)

AUTHOR INFORMATION

Corresponding Author

Andrey M. Markeev − *Moscow Institute of Physics and Technology (National Research University), Dolgoprudny 141701 Moscow region, Russia;* orcid.org/0000-0001-6777-5706; Email: markeev.am@mipt.ru

Authors

Roman I. Romanov − *Moscow Institute of Physics and Technology (National Research University), Dolgoprudny 141701 Moscow region, Russia*

Ivan V. Zabrosaev − *Moscow Institute of Physics and Technology (National Research University), Dolgoprudny 141701 Moscow region, Russia*

Maxim G. Kozodaev − *Moscow Institute of Physics and Technology (National Research University), Dolgoprudny 141701 Moscow region, Russia*

Dmitry I. Yakubovsky − *Center for Photonics & 2D Materials, Moscow Institute of Physics and Technology (National Research University), Dolgoprudny 141700, Russia*

Mikhail K. Tatmyshevskiy − *Center for Photonics & 2D Materials, Moscow Institute of Physics and Technology (National Research University), Dolgoprudny 141700, Russia*

Aleksey A. Timofeev − *National Research Nuclear University MEPhI (Moscow Engineering Physics Institute), Moscow 115409, Russia*

https://doi.org/10.1021/acsomega.2c06794
ACS Omega 2023, 8, 16579−16586

Natalia V. Doroshina − *Center for Photonics & 2D Materials, Moscow Institute of Physics and Technology (National Research University), Dolgoprudny 141700, Russia*
Sergey M. Novikov − *Center for Photonics & 2D Materials, Moscow Institute of Physics and Technology (National Research University), Dolgoprudny 141700, Russia*
Valentyn S. Volkov − *Center for Photonics & 2D Materials, Moscow Institute of Physics and Technology (National Research University), Dolgoprudny 141700, Russia;* orcid.org/0000-0001-8994-7812

Complete contact information is available at: https://pubs.acs.org/10.1021/acsomega.2c06794

Notes

The authors declare no competing financial interest.

■ ACKNOWLEDGMENTS

The main part of the work (experimental setup design and assembly, MoS_2 synthesis, and its general inspection) was supported by the Russian Science Foundation (project no. 19-19-00504-P). Raman and photoluminescence spectroscopy measurements were supported by the Ministry of Science and Higher Education of the Russian Federation (no. 0714-2020-0002). The authors also acknowledge the MIPT Shared Facilities Center for access to the equipment.

■ REFERENCES

(1) Samy, O.; Zeng, S.; Birowosuto, M. D.; El Moutaouakil, A. A Review on MoS_2 Properties, Synthesis, Sensing Applications and Challenges. *Crystals* **2021**, *11*, 355.
(2) Gupta, D.; Chauhan, V.; Kumar, R. A comprehensive review on synthesis and applications of molybdenum disulfide (MoS_2) material: Past and recent developments. *Inorg. Chem. Commun.* **2020**, *121*, 108200.
(3) Khan, M.; Kumar, S.; Mishra, A.; Sulania, I.; Nath Tripathi, M.; Tripathi, A. Study of structural and electronic properties of few-layer MoS_2 film. *Mater. Today: Proc.* **2022**, *57*, 100−105.
(4) Chen, X.; Liu, C.; Mao, S. Environmental analysis with 2D transition-metal-dichalcogenide-based field-effect transistors. *Nano-Micro Letters* **2020**, *12*, 95.
(5) Singh, E.; Singh, P.; Kim, K. S.; Yeom, G. Y.; Nalwa, H. S. Flexible Molybdenum Disulfide (MoS_2) Atomic Layers for Wearable Electronics and Optoelectronics. *ACS Appl. Mater. Interfaces* **2019**, *11*, 11061−11105.
(6) Kim, B.; Kim, J.; Tsai, P.; Choi, H.; Yoon, S.; Lin, S.; Kim, D. Large Surface Photovoltage of WS_2/MoS_2 and MoS_2/WS_2 Vertical Hetero-bilayers. *ACS Appl. Electron. Mater.* **2021**, *3*, 2601−2606.
(7) Xu, T.; Kong, D.; Tang, H.; Qin, X.; Li, X.; Gurung, A.; Kou, K.; Chen, L.; Qiao, Q.; Huang, W. Transparent MoS_2/PEDOT Composite Counter Electrodes for Bifacial Dye-Sensitized Solar Cells. *ACS Omega* **2020**, *5*, 8687−8696.
(8) Kim, K. S.; Ji, Y. J.; Kim, K. H.; Choi, S.; Kang, D.; Heo, K.; Cho, S.; Yim, S.; Lee, S.; Park, J.; Jung, Y. S.; Yeom, G. Y. Ultrasensitive MoS_2 photodetector by serial nano-bridge multi-heterojunction. *Nat. Commun.* **2019**, *10*, 4701.
(9) Sun, Y.; Niu, G.; Ren, W.; Meng, X.; Zhao, J.; Luo, W.; Ye, Z.; Xie, Y. Hybrid System Combining Two-Dimensional Materials and Ferroelectrics and Its Application in Photodetection. *ACS Nano* **2021**, *15*, 10982−11013.
(10) Ramaraj, S. G.; Nundy, S.; Zhao, P.; Elamaran, D.; Tahir, A. A.; Hayakawa, Y.; Muruganathan, M.; Mizuta, H.; Kim, S. W. Sputtered Nb-Doped MoS_2 Thin Film for Effective Detection of NO_2 Gas Molecules: Theoretical and Experimental Studies. *ACS Omega* **2022**, *7*, 10492−10501.
(11) Chen, P.; Hu, J.; Yin, M.; Bai, W.; Chen, X.; Zhang, Y. MoS_2 Nanoflowers Decorated with Au Nanoparticles for Visible-Light-Enhanced Gas Sensing. *ACS Appl. Nano Mater.* **2021**, *4*, 5981−5991.
(12) Sun, J.; Meng, X. Modulating the Electronic Properties of MoS_2 Nanosheets for Electrochemical Hydrogen Production: A Review. *ACS Appl. Nano Mater.* **2021**, *4*, 11413−11427.
(13) Jin, M.; Zhang, X.; Niu, S.; Wang, Q.; Huang, R.; Ling, R.; Huang, J.; Shi, R.; Amini, A.; Cheng, C. Strategies for Designing High-Performance Hydrogen Evolution Reaction Electrocatalysts at Large Current Densities above 1000 mA cm^{-2}. *ACS Nano* **2022**, *16*, 11577−11597.
(14) Wang, J.; Lee, S. A.; Jang, H. W.; Shokouhimehr, M. Emerging Two-Dimensional-Based Nanostructured Catalysts: Applications in Sustainable Organic Transformations. *Langmuir* **2022**, *38*, 9064−9072.
(15) Liang, Z.; Shen, R.; Ng, Y. H.; Zhang, P.; Xiang, Q.; Li, X. A review on 2D MoS_2 cocatalysts in photocatalytic H_2 production. *J. Mater. Sci. Technol.* **2020**, *56*, 89−121.
(16) Ding, Q.; Meng, F.; English, C. R.; Cabán-Acevedo, M.; Shearer, M. J.; Liang, D.; Daniel, A. S.; Hamers, R. J.; Jin, S. Efficient Photoelectrochemical Hydrogen Generation Using Heterostructures of Si and Chemically Exfoliated Metallic MoS_2. *J. Am. Chem. Soc.* **2014**, *136*, 8504−8507.
(17) Zhu, Z.; Mosallanezhad, A.; Sun, D.; Lei, X.; Liu, X.; Pei, Z.; Wang, G.; Qian, Y. Applications of MoS_2 in Li−O_2 Batteries: Development and Challenges. *Energy Fuels* **2021**, *35*, 5613−5626.
(18) Bello, I. T.; Oladipo, A. O.; Adedokun, O.; Dhlamini, S. M. Recent advances on the preparation and electrochemical analysis of MoS_2-based materials for supercapacitor applications: A mini-review. *Mater. Today Commun.* **2020**, *25*, 101664.
(19) Enyashin, A. N.; Yadgarov, L.; Houben, L.; Popov, I.; Weidenbach, M.; Tenne, R.; Bar-Sadan, M.; Seifert, G. New Route for Stabilization of 1T-WS_2 and MoS_2 Phases. *J. Phys. Chem. C* **2011**, *115*, 24586−24591.
(20) Jayabal, S.; Wu, J.; Chen, J.; Geng, D.; Meng, X. Metallic 1T-MoS_2 nanosheets and their composite materials: Preparation, properties and emerging applications. *Mater. Today Energy* **2018**, *10*, 264−279.
(21) Tang, Q.; Jiang, D. Mechanism of Hydrogen Evolution Reaction on 1T-MoS_2 from First Principles. *ACS Catal.* **2016**, *6*, 4953−4961.
(22) Geng, X.; Zhang, Y.; Han, Y.; Li, J.; Yang, L.; Benamara, M.; Chen, L.; Zhu, H. Two-Dimensional Water-Coupled Metallic MoS_2 with Nanochannels for Ultrafast Supercapacitors. *Nano Lett.* **2017**, *17*, 1825−1832.
(23) Tsikritzis, D.; Tsud, N.; Skala, T.; Sygellou, L. Unravelling the phase transition of 2H-MoS_2 to 1T-MoS_2 induced by the chemical interaction of Pd with molybdenum disulfide−graphene hybrids. *Appl. Surf. Sci.* **2022**, *599*, 153896.
(24) Guo, Y.; Sun, D.; Ouyang, B.; Raja, A.; Song, J.; Heinz, T. F.; Brus, L. E. Probing the Dynamics of the Metallic-to-Semiconducting Structural Phase Transformation in MoS_2 Crystals. *Nano Lett.* **2015**, *15*, 5081−5088.
(25) Lin, Y.-C.; Dumcenco, D. O.; Huang, Y.-S.; Suenaga, K. Atomic mechanism of the semiconducting-to-metallic phase transition in single-layered MoS_2. *Nat. Nanotechnol.* **2014**, *9*, 391−396.
(26) Kang, Y.; Gong, Y.; Hu, Z.; Li, Z.; Qiu, Z.; Zhu, X.; Ajayan, P. M.; Fang, Z. Plasmonic hot electron enhanced MoS_2 photocatalysis in hydrogen evolution. *Nanoscale* **2015**, *7*, 4482−4488.
(27) Liu, Z.; Gao, Z.; Liu, Y.; Xia, M.; Wang, R.; Li, N. Heterogeneous Nanostructure Based on 1T Phase MoS_2 for Enhanced Electrocatalytic Hydrogen Evolution. *ACS Appl. Mater. Interfaces* **2017**, *9*, 25291−25297.
(28) Wang, W.; Zeng, X.; Warner, J. H.; Guo, Z.; Hu, Y.; Zeng, Y.; Lu, J.; Jin, W.; Wang, S.; Lu, J.; Zeng, Y.; et al. Photoresponse-Bias Modulation of a High-Performance MoS_2 Photodetector with a Unique Vertically Stacked 2H-MoS_2/1T@2HMoS_2 Structure. *ACS Appl. Mater. Interfaces* **2020**, *12*, 33325−33335.

(29) Singh, A. K.; Kumar, P.; Late, D. J.; Kumar, A.; Patel, S.; Singh, J. Review 2D layered transition metal dichalcogenides (MoS_2): Synthesis, applications and theoretical aspects. *Appl. Mater. Today* **2018**, *13*, 242−270.
(30) Dumcenco, D.; Ovchinnikov, D.; Marinov, K.; Lazic, P.; Gibertini, M.; Marzari, N.; Sanchez, O. L.; Kung, Y.-C.; Krasnozhon, D.; Chen, M.-W.; Bertolazzi, S.; Gillet, P.; Fontcuberta i Morral, A.; Radenovic, A.; Kis, A. Large-Area Epitaxial Monolayer MoS_2. *ACS Nano* **2015**, *9*, 4611−4620.
(31) Tang, L.; Tan, J.; Nong, H.; Liu, B.; Cheng, H.-M. Chemical Vapor Deposition Growth of Two-Dimensional Compound Materials: Controllability, Material Quality, and Growth Mechanism. *Acc. Mater. Res.* **2021**, *2*, 36−47.
(32) Siegel, G.; Venkata Subbaiah, Y. P.; Prestgard, M. C.; Tiwari, A. Growth of centimeter-scale atomically thin MoS_2 films by pulsed laser deposition. *APL Mater.* **2015**, *3*, 056103.
(33) Mahlouji, R.; Verheijen, M. A.; Zhang, Y.; Hofmann, J. P.; Kessels, W. M. M.; Bol, A. A. Thickness and Morphology Dependent Electrical Properties of ALD-Synthesized MoS_2 FETs. *Adv. Electron. Mater.* **2022**, *8*, 2100781.
(34) Keller, B. D.; Bertuch, A.; Provine, J.; Sundaram, G.; Ferralis, N.; Grossman, J. C. Process Control of Atomic Layer Deposition Molybdenum Oxide Nucleation and Sulfidation to Large-Area MoS_2 Monolayers. *Chem. Mater.* **2017**, *29*, 2024−2032.
(35) Romanov, R. I.; Kozodaev, M. G.; Myakota, D. I.; Chernikova, A. G.; Novikov, S. M.; Volkov, V. S.; Slavich, A. S.; Zarubin, S. S.; Chizhov, P. S.; Khakimov, R. R.; Chouprik, A. A.; Hwang, C. S.; Markeev, A. M. Synthesis of Large Area Two-Dimensional MoS_2 Films by Sulfurization of Atomic Layer Deposited MoO_3 Thin Film for Nanoelectronic Applications. *ACS Appl. Nano Mater.* **2019**, *2*, 7521−7531.
(36) Lee, D. H.; Sim, Y.; Wang, J.; Kwon, S.-Y. Metal−organic chemical vapor deposition of 2D van der Waals materials—The challenges and the extensive future opportunities. *APL Mater.* **2020**, *8*, 030901.
(37) Wang, Z.; Shen, Y.; Ito, Y.; Zhang, Y.; Du, J.; Fujita, T.; Hirata, A.; Tang, Z.; Chen, M. Synthesizing 1T−1H Two-Phase $Mo_{1-x}W_xS_2$ Monolayers by Chemical Vapor Deposition. *ACS Nano* **2018**, *12*, 1571−1579.
(38) Tang, J.; Huang, J.; Ding, D.; Zhang, S.; Deng, X. Research progress of 1T-MoS_2 in electrocatalytic hydrogen evolution. *Int. J. Hydrogen Energy* **2022**, *47*, 39771−39795.
(39) Xia, B.; Liu, P.; Liu, Y.; Gao, D.; Xue, D.; Ding, J. Re doping induced 2H-1T phase transformation and ferromagnetism in MoS_2 nanosheets. *Appl. Phys. Lett.* **2018**, *113*, 013101.
(40) Mignuzzi, S.; Pollard, A. J.; Bonini, N.; Brennan, B.; Gilmore, I. S.; Pimenta, M. A.; Richards, D.; Roy, D. Effect of disorder on Raman scattering of single-layer MoS_2. *Phys. Rev. B Condens. Matter* **2015**, *91*, 195411.
(41) Blanco, E.; Afanasiev, P.; Berhault, G.; Uzio, D.; Loridant, S. Resonance Raman spectroscopy as a probe of the crystallite size of MoS_2 nanoparticles. *Compt. Rendus Chem.* **2016**, *19*, 1310−1314.
(42) Feng, Y.; Zhou, W.; Wang, Y.; Zhou, J.; Liu, E.; Fu, Y.; Ni, Z.; Wu, X.; Yuan, H.; Miao, F.; et al. Raman vibrational spectra of bulk to monolayer ReS_2 with lower symmetry. *Phys. Rev. B Condens. Matter* **2015**, *92*, 054110.
(43) Mak, K.; Lee, C.; Hone, J.; Shan, J.; Heinz, T. Atomically Thin MoS_2: A New Direct-Gap Semiconductor. *Phys. Rev. Lett.* **2010**, *105*, 136805.
(44) Splendiani, A.; Sun, L.; Zhang, Y.; Li, T.; Kim, J.; Chim, C.-Y.; Galli, G.; Wang, F. Emerging Photoluminescence in Monolayer MoS_2. *Nano Lett.* **2010**, *10*, 1271−1275.
(45) Kim, J. S.; Kim, J.; Zhao, J.; Kim, S.; Lee, J. H.; Jin, Y.; Choi, H.; Moon, B. H.; Bae, J. J.; Lee, Y. H.; Lim, S. C. Electrical Transport Properties of Polymorphic MoS_2. *ACS Nano* **2016**, *10*, 7500−7506.
(46) Van der Zande, A. M.; Huang, P. Y.; Chenet, D. A.; Berkelbach, T. C.; You, Y.; Lee, G.-H.; Heinz, T. F.; Reichman, D. R.; Muller, D. A.; Hone, J. C. Grains and Grain Boundaries in Highly Crystalline Monolayer Molybdenum Disulphide. *Nat. Mater.* **2013**, *12*, 554−561.
(47) Najmaei, S.; Amani, M.; Chin, M. L.; Liu, Z.; Birdwell, A. G.; O'Regan, T. P.; Ajayan, P. M.; Dubey, M.; Lou, J. Electrical Transport Properties of Polycrystalline Monolayer Molybdenum Disulfide. *ACS Nano* **2014**, *8*, 7930−7937.
(48) Dumcenco, D.; Ovchinnikov, D.; Marinov, K.; Lazic, P.; Gibertini, M.; Marzari, N.; Sanchez, O. L.; Kung, Y.-C.; Krasnozhon, D.; Chen, M.-W.; et al. Large-Area Epitaxial Monolayer MoS_2. *ACS Nano* **2015**, *9*, 4611−4620.
(49) Sharma, C. H.; Surendran, A. P.; Varghese, A.; Thalakulam, M. Stable and scalable 1T MoS_2 with low temperature-coefficient of resistance. *Sci. Rep.* **2018**, *8*, 12463.
(50) Zong, B.; Li, Q.; Chen, X.; Liu, C.; Li, L.; Ruan, J.; Mao, S. Highly Enhanced Gas Sensing Performance Using a 1T/2H Heterophase MoS_2 Field-Effect Transistor at Room Temperature. *ACS Appl. Mater. Interfaces* **2020**, *12*, 50610−50618.
(51) Li, L.; Chen, J.; Wu, K.; Cao, C.; Shi, S.; Cui, J. The Stability of Metallic MoS_2 Nanosheets and Their Property Change by Annealing. *Nanomaterials* **2019**, *9*, 1366.
(52) Krbal, M.; Prikryl, J.; Pis, I.; Prokop, V.; Rodriguez Pereira, J.; Kolobov, A. V. Anomalous electrical conductivity change in MoS_2 during the transition from the amorphous to crystalline phase. *Ceram. Int.* **2023**, *49*, 2619−2625.

https://doi.org/10.1021/acsomega.2c06794
ACS Omega 2023, 8, 16579−16586